

Second-generation dust in planetary systems: The case of HD 163296[★]

Gennaro D’Angelo,^{1†} and Francesco Marzari^{2‡}

¹*Theoretical Division, Los Alamos National Laboratory, Los Alamos, NM 87545, USA*

²*Department of Physics and Astronomy, University of Padova, via Marzolo 8, I-35131, Padova, Italy*

Accepted 2 November 2021. Received 17 October 2021; in original form 23 August 2021

ABSTRACT

Observations indicate that large, dust-laden protoplanetary discs are common. Some features, like gaps, rings and spirals, suggest they may host young planets, which can excite the orbits of nearby leftover planetesimals. Energetic collisions among these bodies can lead to the production of second-generation dust. Grains produced by collisions may have a dynamical behaviour different from that of first-generation, primordial dust out of which planetesimals and planets formed. We aim to study these differences for the HD 163296 system and determine whether dynamical signatures in the mixture of the two dust populations can help separate their contributions. We use three-dimensional (3-D) hydrodynamic models to describe the gaseous disc with three, Saturn- to Jupiter-mass, embedded planets. Dust grains, of sizes $1\ \mu\text{m}$ – $1\ \text{mm}$, are treated as Lagrangean particles with resolved thermodynamics and mass loss. Initial disc and planet configurations are derived from observation-based work, which indicates low gas viscosity. The 3-D approach also allows us to detect the formation of vortices induced by Rossby waves, where dust becomes concentrated and may contribute to planetesimal formation. We find that the main differences in the dynamical behaviour of first- and second-generation dust occur in the vertical distribution. The two populations have similar distributions around the disc mid-plane, although second-generation dust shows longer residence times close to the radial locations of the planets’ gas gaps. Sedimentation rates of μm -size grains are comparable to or lower than the production rates by planetesimals’ collisions, making this population potentially observable. These outcomes can be extended to similar systems harbouring giant planets.

Key words: accretion, accretion discs – methods: numerical — planets and satellites: gaseous planets — planet–disc interactions — protoplanetary discs — stars: individual: HD 163296

1 INTRODUCTION

HD 163296 is a young, Herbig Ae star surrounded by a protoplanetary disc that extends out to at least 450 au (e.g., Wisniewski et al. 2008; Rich et al. 2019). ALMA imaging at millimeter wavelengths detected three concentric, bright ring-like features in the disc (Isella et al. 2016; Muro-Arena et al. 2018), located beyond 50–60 au from the star (see also Rab et al. 2020, and references therein). Concentric dark regions were also detected interior of these bright rings. Observations of a fourth, wider ring (at around 330 au) were reported by Rich et al. (2020). The concentric dark features reflect some amount of depletion, or gaps, in the distribution of dust and gas around the star, whereas bright rings are likely regions of enhanced dust concentration.

One possible mechanism that can produce the observed disc structures relies on the presence of planets at or around those orbital locations. Evolutionary models by Baraffe et al. (2003) suggest luminosity-based detection limits in the range from 1.5 to 4.5 times

Jupiter’s mass, M_J , with a mass limit of $\approx 2 M_J$, for the outer planet (associated to the third gap, Rich et al. 2019). Upper limits of a few M_J for direct imaging were also reported by Mesa et al. (2019). Modelling of the disc dust distribution suggests the presence of smaller, Saturn-mass planets in the second and third gap (Isella et al. 2016). At those same locations, modelling of the gas rotation curves, tracked by CO emission, suggests the presence of $\approx 1 M_J$ planets (Teague et al. 2018). The presence of three planets, in the mass range ≈ 0.5 – $0.6 M_J$, was proposed by Liu et al. (2018) to reproduce observations of the three inner gaps.

In all the cases mentioned above, modelling involved hydrodynamic simulations of disc-planet tidal interactions. It should be pointed out, however, that other physical processes, such as grain growth at condensation fronts of particular gas species, may as well be responsible for the observed ring features (see van der Marel et al. 2018). Moreover, any physical process capable of producing radial variations of the gas turbulence viscosity (see, e.g., Ohashi & Kataoka 2019) or perturbations of the gravity field (e.g., aided by dust back-reaction, Takahashi & Inutsuka 2014) may also be able to produce radial features in the disc.

Current observations of thermal emission suggest that HD 163296 contains dust grains out to about 200 au (e.g., Dullemond et al. 2020). Part of this dust is likely primordial, i.e., it was in the medium out

[★] Accepted for publication in Monthly Notices of the Royal Astronomical Society Main Journal. This version of the manuscript was prepared and typeset by the authors.

[†] E-mail: gennaro@lanl.gov

[‡] E-mail: francesco.marzari@pd.infn.it

of which the system formed. Yet, if giant planets as those predicted by some models exist, second-generation dust may also be found. In fact, the formation of giant planets requires the presence of km-size (and larger) planetesimals (e.g., [Alibert et al. 2018](#); [Voelkel et al. 2020](#); [D'Angelo et al. 2021](#), and references therein), which must have emerged from the primordial dust. Leftover planetesimals that were not incorporated into the planets continue orbiting the star, and those moving in the proximity of the planets have their orbits excited by the planets' gravity. This process may lead to collisional comminution of planetesimals (e.g., [Turrini et al. 2019](#)) and, hence, to the production of second-generation dust.

At an age of 7.6 million years ([Vioque et al. 2018](#)), the primordial dust may have aged to an extent such to render it compositionally different from younger, collisionally-formed dust. Yet, distinguishing the two populations based on composition may prove difficult, if not impossible, since collisions would continuously add new dust to the system and, thus, second-generation grains would have a wide range of ages. The size distribution of the two populations may also be different, but the difference would depend on poorly known details on the outcome of collisional comminution. Coagulation and weathering would also contribute to homogenise the species.

The focus of this study does not rest on the possible compositional or size differences between the two dust populations, but rather on their possible dynamical differences. In fact, gravitational interactions between planetesimals and the planets would raise orbital eccentricity and inclination of the former ([Turrini et al. 2019](#)). Therefore, whereas primordial dust would be expected to orbit mostly in (or close to) the disc mid-plane, and with an eccentricity distribution determined by the gas motion, collisions among planetesimals may generate dust grains with much broader distributions of both eccentricities and inclinations.

One purpose of this study is to analyse, through hydrodynamic modelling, what differences can arise in the distributions of dust species that may represent a primordial population and a second-generation, collisionally produced population of particles, orbiting in the disc region that harbours the predicted planets. Another purpose is to determine the extent to which an admixture of the two populations can bear dynamical signatures that may allow us to separate their contributions.

In the following, we describe the physical properties adopted for the system in Section 2. The computational methods are outlined in Section 3 and the results of the models are described and discussed in Section 4. Our conclusions are presented in Section 5.

2 PHYSICAL DESCRIPTION OF THE SYSTEM

The physical description of the system is mainly based on the work presented by [Isella et al. \(2016\)](#), [Liu et al. \(2018\)](#), and [Turrini et al. \(2019\)](#). We assume a stellar distance $d \approx 122$ pc and a stellar mass $M_\star = 2.3 M_\odot$ (<http://exoplanet.eu>). Although these parameters were revised following Gaia observations, $d = 101.5 \pm 2$ pc and $M_\star = 1.83 \pm 0.09 M_\odot$ ([Vioque et al. 2018](#)), they are nonetheless representative of the system and do not impact the general conclusions of this study, which simply uses HD 163296 as a proxy for a category of protoplanetary discs.

The initial surface density of the disc's gas is approximated to ([Isella et al. 2016](#))

$$\Sigma(t=0) = \Sigma_0 \left(\frac{r_0}{r}\right)^{4/5} \exp\left[-\left(\frac{r}{3.3r_0}\right)^{6/5}\right], \quad (1)$$

in which r_0 is a reference radius that depends on the stellar param-

Table 1. Parameters applied to the cases investigated in this study. The table lists the turbulence parameter α of the disc's gas, the mass of the planets, and their semi-major axes.

Model	Lm α 6	Hm α 5	HmL Σ
α	10^{-6}	10^{-5}	10^{-5}
Σ_0 [g cm $^{-2}$]	14.23	14.23	6.0
m_1/M_\star	1.91×10^{-4}	1.91×10^{-4}	1.91×10^{-4}
m_2/M_\star	1.91×10^{-4}	4.15×10^{-4}	4.15×10^{-4}
m_3/M_\star	2.41×10^{-4}	4.15×10^{-4}	4.15×10^{-4}
a_1/r_0	1.2	1.2	1.2
a_2/r_0	2.1	2.1	2.1
a_3/r_0	3.2	3.2	3.2

ters. Because of the assumed distance, we set $r_0 = 50$ au (the revised distance would result in a smaller value, $r_0 = 41.6$ au). Therefore, one orbital period at $r = r_0$ takes 233.13 years. The reference value of the initial density is $\Sigma_0 = 14.23$ g cm $^{-2}$, and the disc comprises $\approx 0.037 M_\star$ of gas out to 500 au. The power-law used for the surface density profile is somewhat shallower than that adopted by, e.g., [Dullemond et al. \(2020\)](#), although the exponential cut-off is in the range examined by the latter authors. Nonetheless, in light of [Dullemond et al.](#) results, a value $\Sigma_0 = 6.0$ g cm $^{-2}$ is also applied in order to mimic their profile in the region $50 \lesssim r \lesssim 250$ au (note that their total gas mass is $\approx 0.039 M_\star$, close to the value stated above).

The temperature structure in the disc, taken as height-independent, is

$$T = T_0 \sqrt{\frac{r_0}{r}}, \quad (2)$$

in which $T_0 = 33.94$ K, as the mid-plane temperature chosen by [Isella et al. \(2016\)](#). We note that shallower temperature profiles have been proposed for this system. In particular, [Flaherty et al. \(2015\)](#) proposed a temperature power index ≈ 0.3 whereas [Dullemond et al. \(2020\)](#) proposed a much flatter profile, $T \propto (1/r)^{0.14}$. Nonetheless, the latter authors estimated a mid-plane temperature at $r \approx 100$ au of about 25 K, only a few degrees lower than the temperature applied here. Equation (2) places the ice sublimation line at around 2.5 au ($T \approx 150$ K), at which radial location 1 mm ice particles would take less than an orbital period to evaporate.

According to Equation (2), the disc is flared and its aspect ratio is given by

$$h = h_0 \left(\frac{r}{r_0}\right)^{1/4}, \quad (3)$$

where $h_0 = 0.0537$. The initial density of the gas scales as $\rho \propto \Sigma/H$ in the radial direction and as $\rho \propto \exp[-(\cot \theta/h)^2]$ in the meridional direction (θ is the co-latitude angle, $\theta = \pi/2$ at the mid-plane).

We apply a simple prescription for the kinematic viscosity of the disc's gas, $\nu = \alpha H^2 \Omega$, where $H = hr$ is the pressure scale-height, Ω is the Keplerian orbital frequency of the gas, and α is the Shakura & Sunyaev turbulence parameter ([Shakura & Sunyaev 1973](#)). Disc models have been proposed in which α varies with radius (e.g., [Isella et al. 2016](#); [Liu et al. 2018](#)). Here we opt for a constant α since this study does not test different viscosity prescriptions or temperature distributions.

It is assumed that three planets orbit in the disc, with orbital radii as indicated in Table 1. We consider three basic scenarios, two of which (Lm α 6 and Hm α 5) by varying the mass of the planets ("low" and "high" masses, see [Turrini et al. 2019](#)) and the α parameter, in the range of values considered by [Liu et al. \(2018\)](#). In particular, the favoured model of the latter authors predicts depletion factors in the gas density gaps around the inner two planets of somewhat less than

10 and 3, respectively (and smaller still around the third planet). Note that these authors used a colder gas to model the disc, which is more prone to open gaps by tidal torques. As mentioned, a third model also considers a lower gas surface density ($H\mu L\Sigma$) which may affect dust dynamics. This model may also be viewed as representing a later stage in the evolution of the system (i.e., an older, more depleted disc). The planets interact gravitationally among themselves and with the star. They act on the disc (gaseous and solid component) but do not feel the disc's gravity.

3 COMPUTATIONAL METHODS

We use the numerical methods described in [D'Angelo & Marzari \(2012\)](#), and references therein) to model the gas evolution and those presented in [D'Angelo & Podolak \(2015\)](#) to model the evolution of solids. These methods were also applied in [Marzari et al. \(2019\)](#) and are briefly outlined in the next two sections.

3.1 Gas Evolution

The evolution of the gaseous disc is simulated by means of three-dimensional (3D) hydrodynamic calculations. We use a spherical polar reference frame $\{O; R, \theta, \phi\}$ whose origin O is attached to the star. Quantity R indicates the polar radius whereas $r = R \sin \theta$ is the cylindrical radius. The disc domain extends radially from $r = 0.1 r_0$ to $10 r_0$ and 2π in azimuth (ϕ) around the star. The co-latitude angle θ is $\leq \pi/2$ and the disc is symmetric relative to its mid-plane, $\theta = \pi/2$. The disc extends 12° above the mid-plane, thus including about 4 pressure scale-heights H at the reference radius r_0 . The coordinate system rotates around the axis $\theta = 0$, perpendicular to the mid-plane, at a constant angular velocity $\Omega_f = \sqrt{GM_\star/r_0^3}$.

The gravitational potential in the disc is given by

$$\Phi = \Phi_\star + \sum_n \Phi_n + \Phi_I, \quad (4)$$

where $\Phi_\star = \sqrt{GM_\star/R^3}$ is the star's potential, Φ_n is the potential generated by planet “ n ”, and Φ_I is the indirect potential due to non-inertial forces caused by the motion of the system's origin, O . To avoid singularities, the potential Φ_n includes a softening length equal to $1/5$ of the planet's Hill radius.

The equations of motion of a viscous fluid are solved with an Eulerian, finite-difference code that is second-order accurate in both space and time. Orbital advection ([Masset 2000](#)) is applied to increase the time-step of the calculations (see [D'Angelo & Marzari 2012](#)). The disc is represented by a grid comprising $662 \times 22 \times 422$ grid cells, in the R , θ , and ϕ direction, respectively. Reflective boundary conditions are applied at both radial boundaries and at the disc surface, whereas symmetry boundary conditions are applied at the mid-plane. The equations of motion of the planets in the disc are solved in the rotating reference frame as discussed in [D'Angelo & Marzari \(2012\)](#). Although some amount of gas accretion on the planets is expected, accretion of gas is neglected (and largely irrelevant for the purposes of this study).

To gauge resolution sensitivity, some portions of the evolution were also performed at a higher resolution, $1332 \times 42 \times 842$ grid elements, for each of the three models in [Table 1](#). Comparisons of the results at the two resolutions yield good agreement (see discussion in [Appendix A](#)).

3.2 Solids' Evolution

Solids are treated as Lagrangian particles. They interact with the gas, the star and the planets, but not with each other. Therefore, results can be re-scaled to an arbitrary number of particles, as long as the solids' mass is small compared to the gas mass in each grid cell. The calculations model particle dynamics, its thermal state, and mass evolution (through evaporation, for details see [D'Angelo & Podolak 2015](#)). Dust is assumed to be ice (mass density $\rho_s = 1 \text{ g cm}^{-3}$), although an admixture containing a small percentage of silicates is expected to result in a similar dynamical and thermal behaviour.

The initial distribution of dust comprises 22400 particles, equally distributed in four size bins of radius $R_s = 1 \mu\text{m}$, $10 \mu\text{m}$, $100 \mu\text{m}$, and 1 mm . This range of sizes is supported by radiative transfer modelling of HD 163296 (e.g., [Ohashi & Kataoka 2019](#)). A simulation with a higher number of particles is presented in [Appendix A](#). The comparison with the case modelling fewer particles yields consistent outcomes and indicates that the particle number does not introduce any significant bias. Details and further discussion on the initial distributions of the particles' eccentricity, e_s , and inclination, i_s , are also provided in the Appendix, including a test on the orbital excitation of planetesimals via interactions with the planets. Although collisions are not modelled, we tested that the orbits of planetesimals in the disc's planet region become readily eccentric and inclined.

Solids that move close to the planets, within about 1.6 times the current radius of Jupiter, are regarded as accreted and removed from the calculation. Giant planets can achieve these radii during their contraction phase, when gas accretion is limited by the disc supply (e.g., [Lissauer et al. 2009](#); [D'Angelo et al. 2021](#)), as expected for the age of this system.

The production of dust is not modelled in this study. It is assumed that collisional comminution of planetesimals leads to fragmentation down to small scales, so that μm - to mm -size grains are generated. No assumption is made on mass partition among various grain sizes although, as discussed in the next sections, dust at the lower end of the range is more likely to trace its origin (i.e., first- versus second-generation). It is worth noticing that calculations modelling planetesimal impacts do not necessarily capture the full size distribution of the fragments arising from collisions, from hundreds of kilometres (or more) to microns (or less). For example, [Weidenschilling \(2010\)](#) computed the collisional evolution of large planetesimals down to metre-size bodies and then extrapolated the size distribution to μm -size grains. [Turrini et al. \(2019\)](#) applied a similar approach and our working hypothesis relies on these results.

4 RESULTS

4.1 Planet-Induced Perturbations

The gas density distribution along a planet's orbit, in a disc with finite viscosity, remains unperturbed as long as viscous torques exceed the tidal torques generated by the planet's gravity. However, for low enough viscosity and/or large enough planet mass, tidal torques can overpower viscous torques.

Conservation of the gas radial momentum (and ignoring viscous stresses and self-gravity) implies that the azimuthal velocity in the disc mid-plane is such that

$$u_\phi^2 \approx v_{\text{Kep}}^2 + \left(\frac{r}{\rho}\right) \frac{\partial p}{\partial r}, \quad (5)$$

where the gas pressure is $p = c^2 \rho$ and $c = hv_{\text{Kep}}$ is the gas sound speed. If the disc is unperturbed (e.g., without planets) and ρ is a

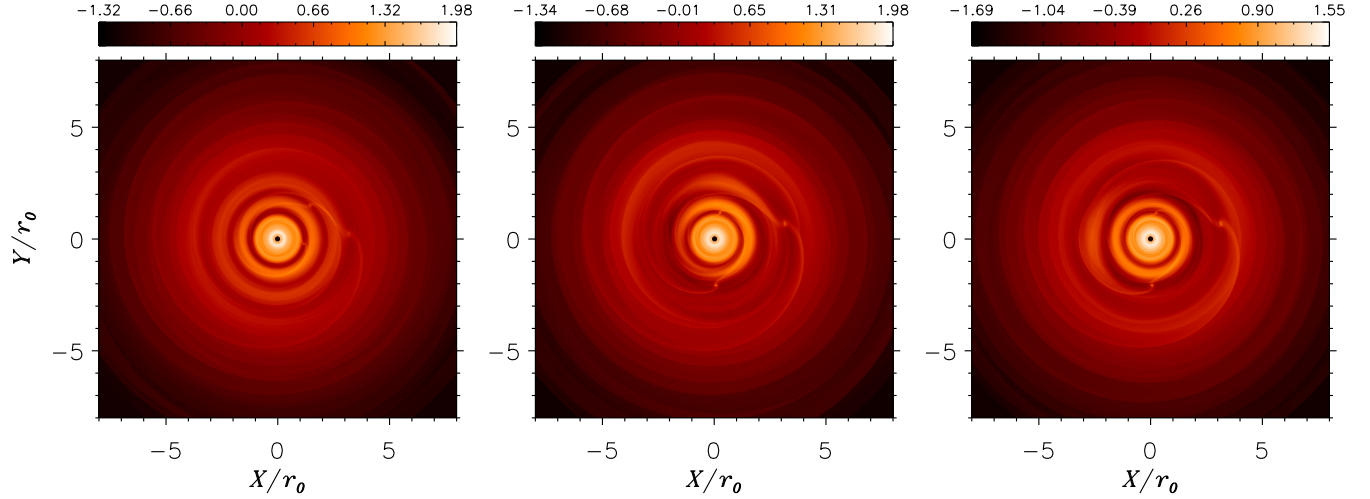


Figure 1. Gas surface density (Σ) after 2600 orbital periods of evolution at $r = r_0$ ($t \approx 6 \times 10^5$ years) in model Lm α 6 (left), Hm α 5 (centre), and HmL Σ (right). The colour scale represents $\log \Sigma$, where Σ is in units of g cm^{-2} .

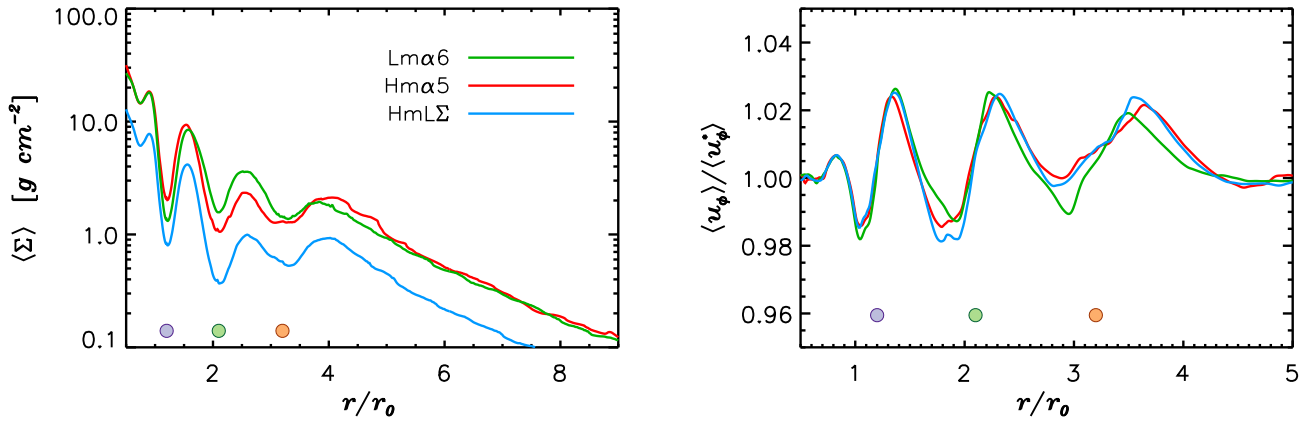


Figure 2. Left: Surface density of the gas, averaged in azimuth around the star, as a function of the radial distance from the star for the three cases listed in Table 1. The symbols indicate the planets' orbital radius, in units of the reference distance, r_0 . Right: Ratio of the gas azimuthal velocity to its unperturbed value (i.e., without planets), averaged around the star for the density distributions displayed in the left panel.

power-law of the radial distance r , the derivative term in Equation 5 is $\propto (h\nu_{\text{Kep}})^2$.

The planets listed in Table 1 have normalized Hill radii $R_H/r = \sqrt[3]{m_p/(3M_\star)}$ comparable to, but somewhat smaller than, the disc aspect ratios at the planets' locations (which increase outward). The effects of the tidal perturbations can be seen in Figure 1, which show $\Sigma(r, \phi)$ for the three models after 2600 orbits at r_0 . The surface density averaged azimuth is displayed in the left panel of Figure 2. The curves show gaps in the gas distribution with depths comparable to those in Figure 7 of Liu et al. (2018), obtained from two-dimensional (r - ϕ) simulations.

In a disc that is tidally perturbed by planets, gap formation alters the density gradient $\partial\rho/\partial r$ around the gap edges, and hence the gas pressure gradient, so that u_ϕ also becomes perturbed and can rise above or drop below its unperturbed value, u_ϕ^* , depending on the sign of $\partial\rho/\partial r$. The right panel of Figure 2 shows the ratio u_ϕ/u_ϕ^* , averaged in azimuth around the star. Deviations of the gas rotation

profile from a Keplerian pattern have been reported for HD 163296 by several groups (e.g., Teague et al. 2018; Pinte et al. 2018; Rab et al. 2020), based on observations of CO spectral features. In particular, Teague et al. (2018) obtained fractional deviations of a few percent in the region occupied by the second and third planet, between ≈ 80 and ≈ 200 au, in good accord with the results presented in the Figure (note that we refer to the unperturbed velocity u_ϕ^* rather than to the Keplerian velocity v_{Kep}). Rab et al. (2020) also performed a detail analysis of the rotational velocity deviations of the ring region and arrived at very similar conclusions (see total fractional variations in their Figure 7). Pinte et al. (2018) reported deviations at ≈ 260 au amounting to $\approx 15\%$ of the local Keplerian velocity, which they modelled as induced by a $2 M_J$ planet orbiting at that distance. Since a massive planet at said location is absent in our setup, this feature is not produced. However, the models in Figure 2 confirm that local deviations from Keplerian rotation of the gas velocity in the proximity

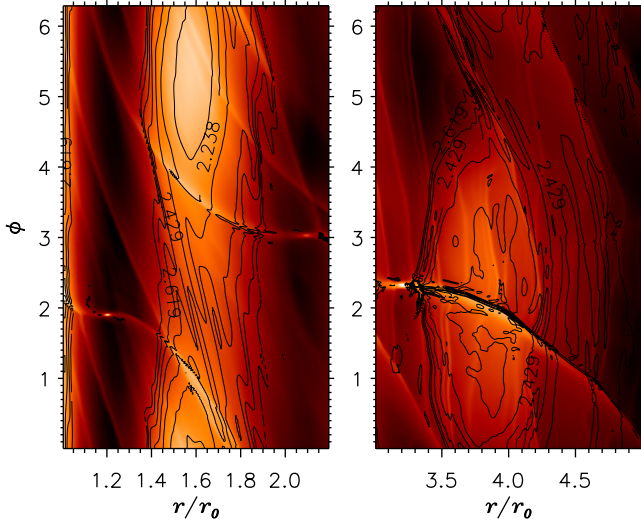


Figure 3. Surface density (colour scale) exterior to the inner (left) and outer planet (right) in model Lm α 6. The black contours represent the potential vorticity of the gas, Equation 6, and indicate the presence of vortices. In the left panel, the vortex spans an azimuthal angle of about π , and somewhat larger in the right panel (traversed by a spiral wave through the middle).

of the second and third planet (whose masses here are between ≈ 0.5 and $\approx 1 M_J$) can reach levels of 10%.

Solid grains have a tendency to concentrate in regions where $\langle u_\phi / u_\phi^* \rangle > 1$, although more localised features in the gas distribution, such as vortices, can alter the process. A clear example is presented in the Appendix, Figure A2, which compares dust distributions for disc models with different levels of gas turbulence. Note that in the cases displayed in Figure 2, the local maxima of $\langle u_\phi / u_\phi^* \rangle$ occur somewhat inward of the local maxima in azimuth-averaged surface density.

4.2 Vortex Formation and Dust Distribution

Rossby waves in thin Keplerian discs (see, e.g., Lovelace et al. 1999; Tagger 2001) can enter a non-linear regime and promote the formation of vortices (see, e.g., Li et al. 2001) which, if persistent, may confine small solids (e.g., Barge & Sommeria 1995; Bracco et al. 1999). In the case of vortices arising from planet-induced perturbations in two-dimensional discs, Fu et al. (2014) found that low levels of turbulent viscosity are required, corresponding to $\alpha \lesssim 10^{-4}$, for disc aspect ratios comparable to those applied here. Consistent with those findings, the three-dimensional models in Table 1 all show the emergence of vortices exterior to the planets’ orbits, as displayed in Figure 3. The potential vorticity of the flow,

$$\zeta = (\nabla \times \mathbf{u}) \cdot \hat{\mathbf{z}} / \Sigma \quad (6)$$

(\mathbf{u} is the gas velocity in an inertial frame), is displayed as contour levels, overlapped to the surface density (colour scale), exterior to the orbits of the inner (left panel) and outer planet (right panel). The vortices span an angle $\gtrsim \pi$ in azimuth. In three dimensions, vortices are expected to also have a vertical structure (e.g., Meheut et al. 2012). The presence of a similar feature exterior to the second planet, based on the contours of ζ , is less evident due to the interference of spiral waves propagating through the region.

Figure 4 shows radius and azimuth (projected) positions of the particles in the lower panels and the radial and meridional (projected) positions in the upper panels, over $3 H$, for model Lm α 6. Particles are colour-coded by size. The dynamical behaviour of the particles orbiting exterior to the planets’ orbits are consistent with the presence of vortical motions in the gas. The largest solids, $R_S = 100 \mu\text{m} - 1 \text{ mm}$, which move relative to the gas by drag on the shortest timescales, tend to be concentrated toward the centres of the vortices. Over the evolution of these models, the effect appears most evident for 1 mm solids, which are collected in regions with high concentrations relative to their surroundings, but smaller particles are affected as well, especially when close to the mid-plane (compare particle distributions around the outermost vortex in the left and right panel of Figure 4). Note that the motion of dust clearly indicate the presence of a vortex also between the two outermost planets. The confinement of dust in radius and azimuth, for various sizes, can be evaluated more quantitatively in the histogram of Figure 5 (left panels), in which different colours represent populations of different radii. The 1 mm solids show sharp peaks around the locations of the vortex centres. By the end of the simulation, the peak concentration of these particles is between 10 and 40 times as large as in the initial concentration at those locations. The distributions of orbital eccentricity of the particles (centre panels) are governed by the eccentric motion of the gas (driven by tidal interactions with the planets, e.g., Ogilvie & Lubow 2003; D’Angelo et al. 2006), which dictates values significantly larger than those of the planets (see symbols). The eccentricities of collisionally-produced dust decay relatively quickly, and therefore would not be useful to probe the origin of the two dust species (compare top and bottom panels).

A behaviour similar to that of model Lm α 6 for the confinement and distribution of dust is observed in the other model configurations (see Figures 6 and 8). The cases better show that also $\sim 1 \mu\text{m}$ grains are collected within the vortices over the duration of the simulations (see left panels). Experiments conducted at higher viscosity, $\alpha = 10^{-3}$, for both configuration of the planet masses, indicate no such features exist (an example is presented in Appendix A, Figure A2).

Although the long-term evolution of vortices was not monitored in detail, these features did persist for the duration of the calculations. We do not speculate on the fate of the solids’ concentrations, which is not simulated in the models (since particles are treated as single physical units, not as super-particles), although above some threshold they may collapse into larger solids (e.g., Heng & Kenyon 2010; Cuzzi et al. 2010, and references therein). It is expected that both first- and second-generation dust orbiting close to the disc mid-plane would be affected by vortices in a similar manner, and therefore they would not provide an indicator to distinguish the two populations. Aside from the presence of these flow features, which requires particular conditions (e.g., low α and low gas temperatures), the conclusion stemming from the mid-plane gas dynamics is more general: it may affect dust differently based on their size but not on their origin, as can also be concluded by comparing the semi-major axis and eccentricity distributions in the upper and lower panels in Figures 7 and 9. Some differences can be seen in the presence of dust within the gas gaps generated by the planets, which take longer to be cleared when grains are initially distributed off the mid-plane (see, e.g., left panels of Figure 5), an effect connected to their settling timescale. The extended clearing time in gaps, added to the continued production of second-generation dust could help explain some observations (e.g., Isella et al. 2016) and also affect the estimates of turbulence levels in the gas. Note that the right panels of Figures 4, 6, and 8 show that particles approach the star closer than those in the left panels. This is because of the smaller perihelia (larger e_s on average) of the

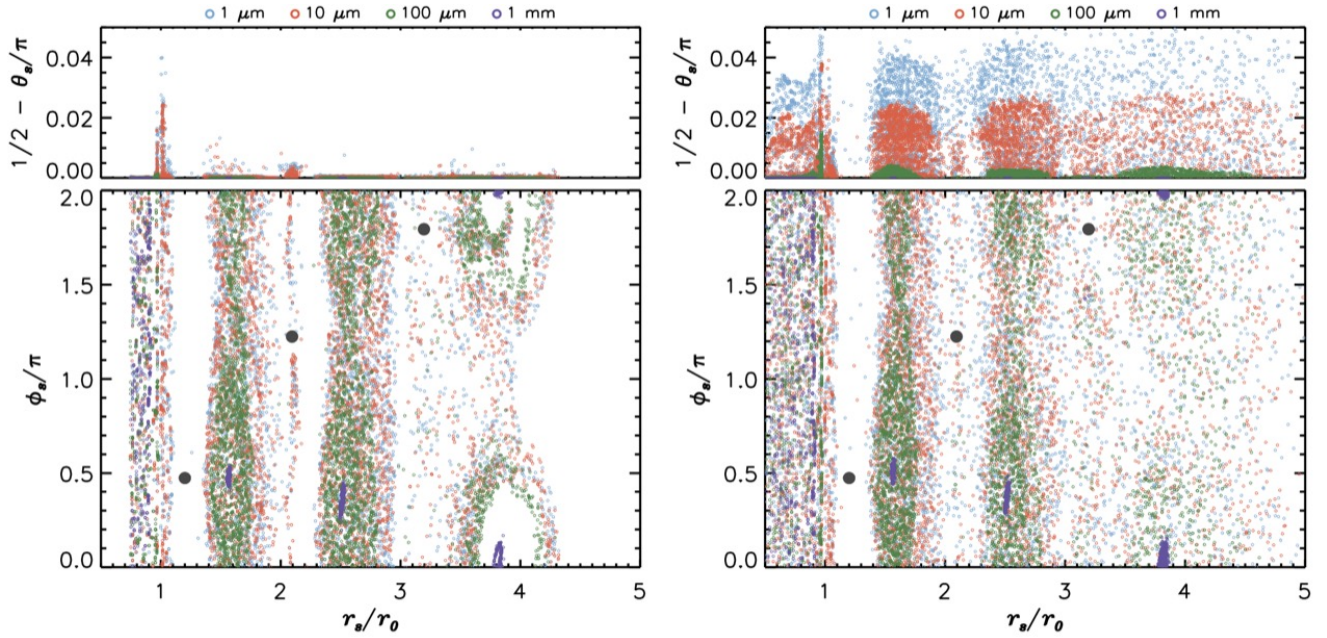


Figure 4. Distribution of solid particles 500 orbits after injection ($t = 3000$ orbits at $r = r_0$) in model Lm α 6. Top and bottom panels show the particles' positions projected in the r - θ and r - ϕ planes (in the top panels the angle is relative to the mid-plane, $\theta = \pi/2$, increasing northward). Different colours refer to different particle radii, as indicated in the legend. The grey solid circles represent the planets. Left panels refer to the simulation in which dust is released in the disc mid-plane whereas right panels refer to the model in which dust is produced via planetesimals' collisions. (*High-resolution versions of this figure can be found [here](#).*)

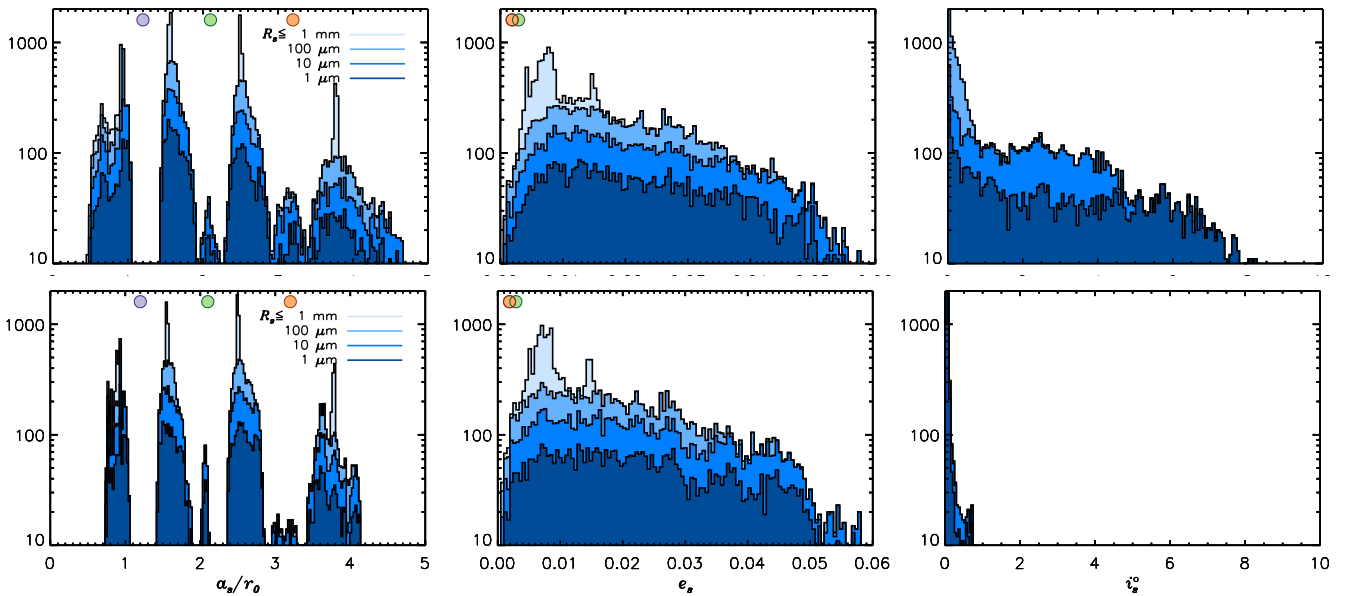


Figure 5. Histograms of the particles' distribution at $t = 3000$ orbits, 500 orbits after injection, for models Lm α 6. Top/bottom panels show models with collision-produced/first-generation dust. From left to right, the histograms display the distributions of semi-major axis, orbital eccentricity, and inclination. Different shades of blue refer to different ranges of particle radii, as indicated in the legend (lightest shade for the total distribution and darkest shade for the smallest particles). The coloured circles represent the planets semi-major axis (left panels) and orbital eccentricity (centre panels).

initial distribution of second-generation particles (see top panels of Figure A1).

Removal of dust by sublimation is negligible in these models. Since the inner boundary of the computational domain only extends inward to 4–5 au (depending on r_0), ablation of ice by thermal radiation is ineffective (e.g., D'Angelo & Podolak 2015). Nonetheless, a small

fraction the modelled solids' mass (0.1–1%) evaporates. This is likely due to frictional heating undergone by some particles in the proximity of the planets, where both ρ and relative velocities (between gas and solids) are enhanced (in fact, the loss is greatest in model Hm α 5). Accretion on the planets removes up to a few percent of the modelled solids' mass. Both removal processes affect the two dust populations

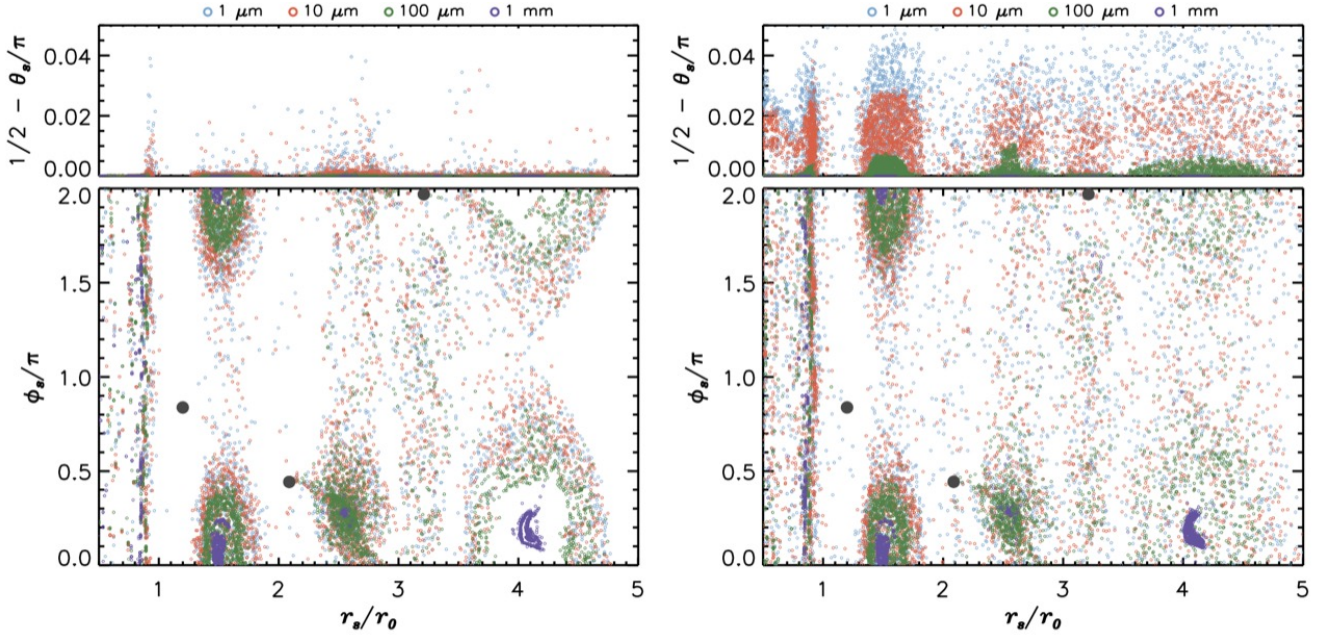


Figure 6. As Figure 4, but the solids’ distributions refer to model Hm α 5. Left panels show results from the simulation in which dust is released in the disc mid-plane whereas right panels show results from the simulation in which dust is produced by planetesimals’ collisions. (*High-resolution versions of this figure can be found [here](#).*)

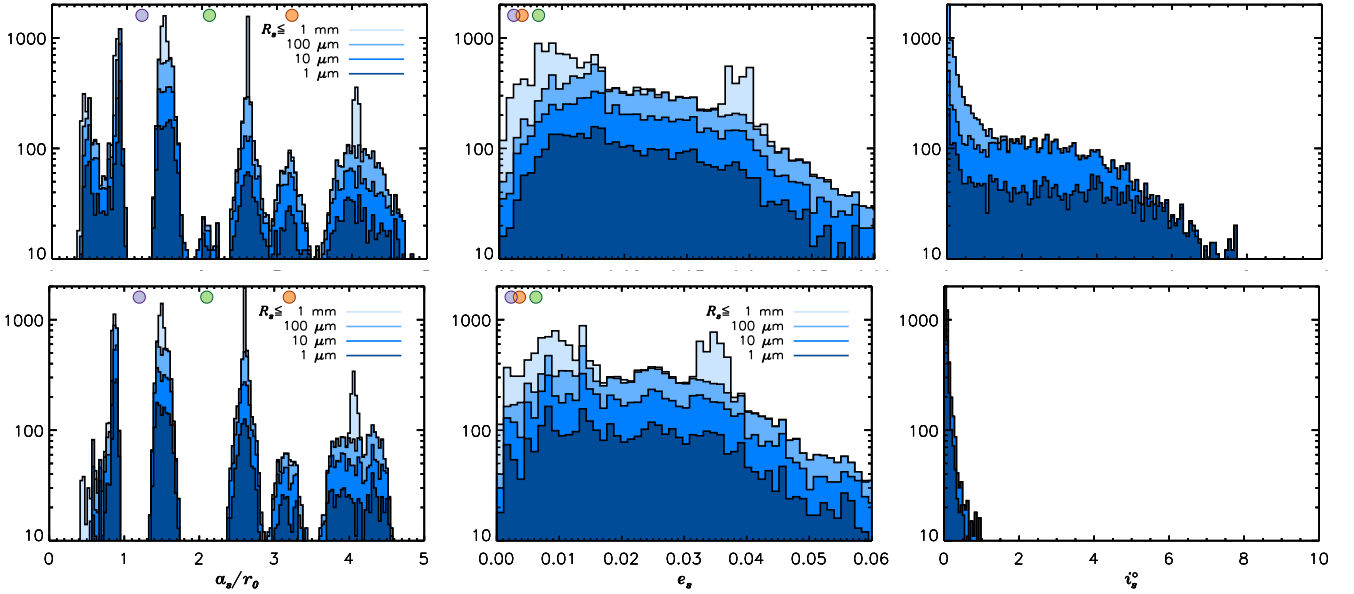


Figure 7. As Figure 5, but for models Hm α 5. Top and bottom panels show results for collision-produced and first-generation dust, respectively. Different shades of blue render different particle radii, as indicated.

to a similar extent, implying that the largest grains (which orbit closest to the mid-plane) are mainly involved.

4.3 Dust Vertical Settling

The largest dynamical differences between the two scenarios representing first- and second-generation dust are, as expected, found in the vertical distributions of the smallest particles, $R_s = 1\text{--}10\ \mu\text{m}$, which take the longest to settle toward the mid-plane of the disc compared

to larger grains (see upper panels of Figures 4, 6 and 8). After a period of a few hundreds of orbits, $R_s = 100\ \mu\text{m}\text{--}1\ \text{mm}$ particles are mostly confined in (or in the proximity of) the mid-plane. These and larger grains would quickly mix with primordial mid-plane dust.

In a disc unperturbed by planets, assuming that the (spherical) grains are within the Epstein regime of gas drag (i.e., R_s is much smaller than the mean-free path of gas atoms/molecules) and their velocity relative to the gas remains subsonic, the stopping time of the particles (i.e., their relative velocity divided by the drag acceleration)

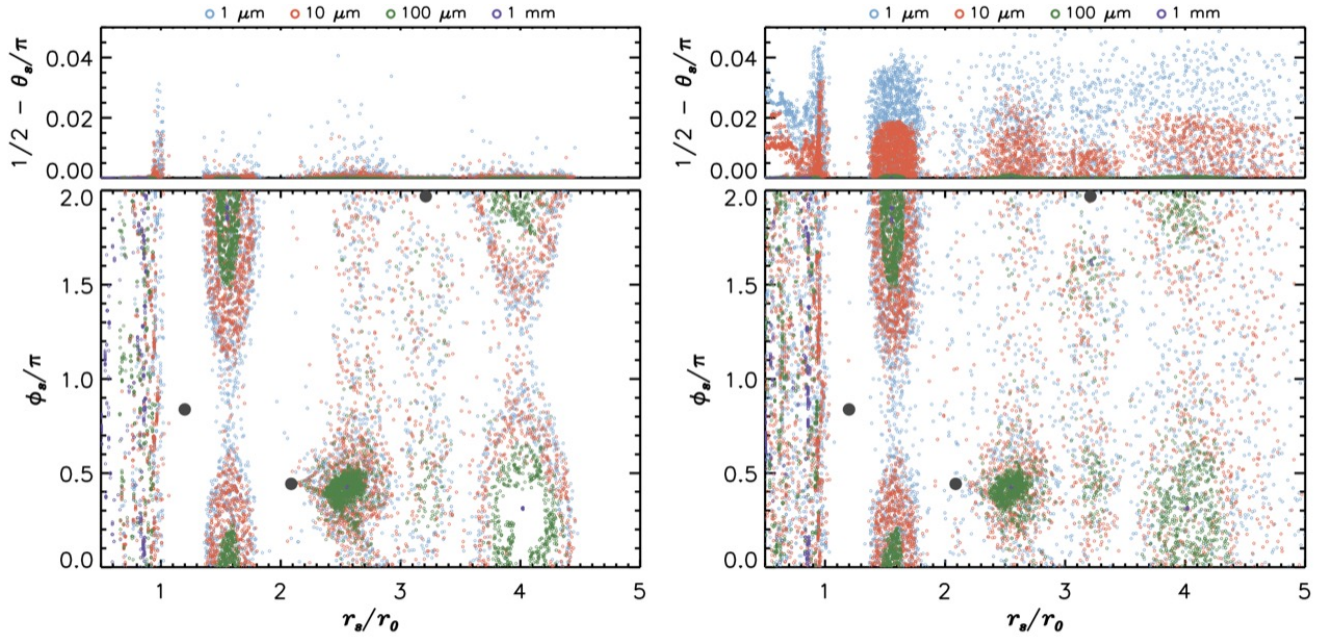


Figure 8. As Figure 4, but the solids' distributions refer to model Hm Σ . Left and right panels show, respectively, results from the models in which dust is released in the disc mid-plane and in which dust is assumed to arise from planetesimals' collisions. (*High-resolution versions of this figure can be found [here](#).*)

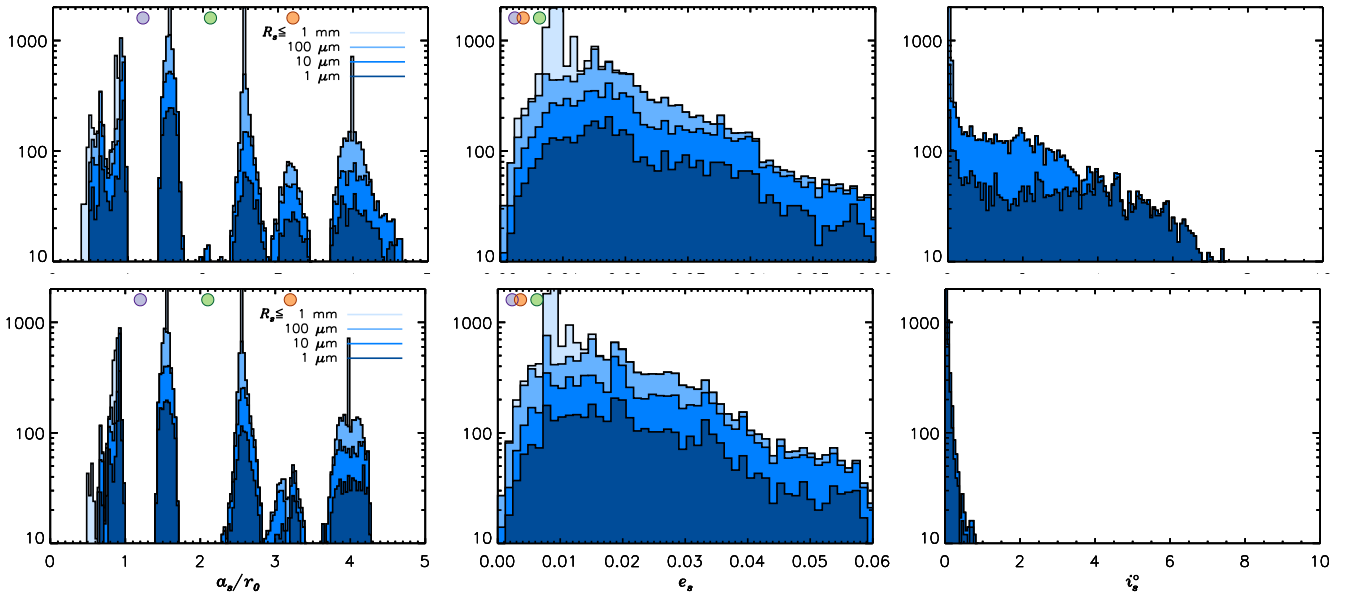


Figure 9. As Figure 5, but for models Hm Σ . Top/bottom panels show simulations with collision-produced/first-generation dust. Different shades of blue render different particle radii, as indicated.

is

$$\tau_{\text{stop}} = \left(\frac{\rho_s}{\rho} \right) \left(\frac{R_s}{c} \right), \quad (7)$$

in which ρ is the gas density (and c the sound speed). The stopping time increases as the particle size increases and the gas density reduces. The dust settling timescale, τ_{set} , is given by the distance over the mid-plane, z , divided by the settling velocity, $|v_{\text{set}}| = z\Omega_K^2\tau_{\text{stop}}$

(see, e.g., [Dullemond & Dominik 2004](#)), so that

$$\Omega_K\tau_{\text{set}} = \frac{1}{\Omega_K\tau_{\text{stop}}}. \quad (8)$$

Therefore, as τ_{stop} approaches zero, the settling timescale diverges since dust tends to move as a parcel of gas. At a given radius in the disc, expanding the gas density in Equation (7), this timescale is

$$\Omega_K\tau_{\text{set}} \propto \frac{1}{R_s} \left(\frac{\Sigma}{\rho_s} \right) \exp \left[- \left(\frac{\cot \theta}{h} \right)^2 \right], \quad (9)$$

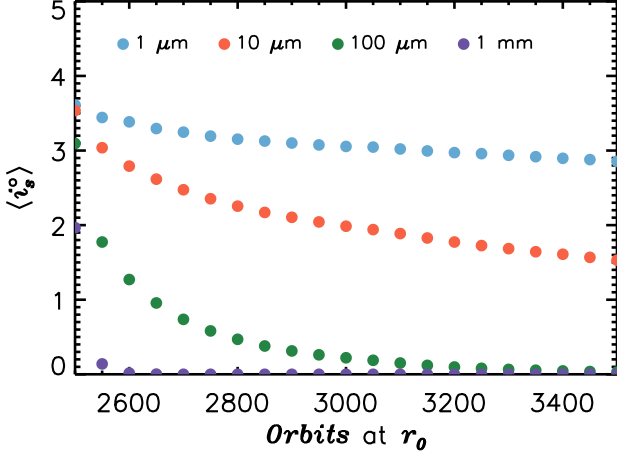


Figure 10. Average orbital inclination of dust grains, for different radii (as indicated), as a function of time for model Lm̑6. The dust is released in the disc at $t \approx 2500$ orbits (the time refers to the reference radius r_0). The average includes solids at all orbital radii.

where $\cot \theta = z/r$ (r is the cylindrical radius). Dust grains decay very quickly far above the disc mid-plane because of low gas density (hence, long τ_{stop}) but τ_{set} becomes nearly independent of height below the gas pressure scale-height, H .

The expectation is that the settling timescale locally drops as the particle size increases, which is in agreement with the dust inclination distributions in the right panels of Figures 5, 7 and 9. It should be noted, however, that Equations (7), (8), and (9) are of limited application in the interpretation of the simulation results since settling grains of a given size may be outside of the Epstein drag regime as gas density increases toward the mid-plane. In addition, since second-generation dust evolves in a disc perturbed by planets, the sedimentation velocity is also affected by their presence (directly through their gravity and indirectly through perturbations induced in the gas flow). Therefore, the settling timescale can be different, or somewhat different, from that predicted by the analytical estimate (in the applicable size range) provided by Equation (8). In fact, the top-left panels of Figures 4, 6 and 8 all indicate that the planets cause some amount of vertical stirring on the mid-plane dust, mostly confined to radial locations in the proximity of the planets’ orbits. Since the effect appears larger on the small grains, it is mainly associated to the vertical motion of the gas induced by the planets. From the inclination distributions in the bottom panels of Figures 5, 7 and 9, the bulk vertical stirring (including particles of all sizes) in the disc region perturbed by the planets can be estimated to not exceed $\approx 25\%$ of gas scale-height. This estimate depends on the planet masses (and gas temperature) considered herein and would be enhanced if more massive planets were perturbing the gas. Obviously, this effect would equally impact first- and second-generation dust. Nonetheless, vertical stirring of dust by planets could potentially influence the interpretation of observations constraining the gas-to-dust scale-heights (see, e.g., Ohashi & Kataoka 2019; Doi & Kataoka 2021).

4.4 Dust Sedimentation and Replenishment

The sedimentation behaviour of dust is more clearly observed in Figure 10, which presents the average orbital inclination of the grains versus time, in model Lm̑6, for the various particle sizes. A very similar settling behaviour is found in model Hm̑5. The averages are computed as mean values of the entire population of solids (binned by grain radius), including all orbital radii ($0.5 r_0 \lesssim a_s \lesssim 4.5 r_0$). Clearly, the presence of small dust off the disc mid-plane would depend on the balance between sedimentation and replenishment by collisional comminution of planetesimals. If the latter process occurred on a timescale comparable to (or shorter than) those involved in Figure 10, then dust would be distributed, and possibly observable, over a range of heights. It should be noted that turbulent stirring would not contribute significantly to the dust vertical distribution because of the low values of the parameter α employed herein (e.g., Dubrulle et al. 1995). These low turbulence values, however, appear to be consistent with the observed structures of the dust in the disc mid-plane (e.g., Isella et al. 2016; Liu et al. 2018). Weak turbulence is also supported by observations of CO emission lines (Flaherty et al. 2015).

Figure 10 shows, as expected, that the initial decline of the dust inclination is rapid at heights $\gtrsim H$ but it slows down as grains approach the mid-plane. The mean settling timescales, evaluated over the last ≈ 800 orbits of evolution from the data plotted in the Figure, are ≈ 6700 and ≈ 1700 orbits (at r_0) for $R_s = 1$ and $10 \mu\text{m}$, respectively. These timescales are determined by fitting an exponential curve to the average dust inclination, so that $d\langle i_s \rangle/dt = -\langle i_s \rangle/\tau_{\text{mod}}$ and τ_{mod} is the model estimate of the settling timescale. As anticipated above, τ_{mod} represents a bulk value that includes particles at all radial distances in the distribution (see, e.g., Figures 4 and 5), and therefore accounts for variations associated to the varying gas density. Larger grains settle, on average, on timescales shorter than 250 orbits. Model Hm̑L, with lower gas density (hence longer stopping times), provides shorter settling timescales, between $\tau_{\text{mod}} \approx 5100$ ($R_s = 1 \mu\text{m}$) and 1000 ($R_s = 10 \mu\text{m}$) orbits.

According to the calculations of Turrini et al. (2019), collisions among planetesimals, whose orbital dynamics is excited by the planets’ gravity, would produce and distribute dust over many gas scale-heights. In the presence of fully formed (Jupiter-mass) planets, that study estimated average dust production timescales by collisions of 6200–6600 orbits (at r_0). These would be average values over the planetary region, but production rates also depend on orbital distance and decline with r . Sedimentation would bring this dust down to heights $\approx H$ on relatively short times, as models indicate, but further settling of $\approx 1 \mu\text{m}$ (and smaller) grains would occur on timescales comparable with dust resupply by collisions. Henceforth, a population of small dust distributed above the mid-plane, up to $\approx H$, would be expected if planetesimal collisions were ongoing.

The production of second-generation dust would depend on several quantities, such as number density of planetesimals, their size distribution, and the interior strength of the bodies. Collision rates would also depend on the planets’ masses. Higher/lower gas densities in the disc could affect dust dynamics, but much less planetesimal collisions. Nonetheless, if the parameters applied here are representative of HD 163296 system, based on the settling timescales of small grains, resupply of dust should occur over timescales $\lesssim 1.5$ Myr in order for second-generation dust to be observable above the disc mid-plane. Over longer collisional timescales, this dust population would likely be completely mixed with primordial dust. The admixture of the two populations, whose orbits would be largely confined to the disc mid-plane, would show similar dynamical features (including

some vertical stirring by the planets) and would not offer distinctive dynamical signatures for separating the two species. A lack of indicative features would also be expected if collisions were unable to produce significant quantities (from an observational point of view) of $\lesssim 10\ \mu\text{m}$ grains, although the size limit would depend on the thermodynamic properties of the gas.

Multi-wavelength observations of HD 163296 (Muro-Arena et al. 2018) indicate that although three rings are detectable in millimetre thermal emission, only the innermost ring is detectable in polarised scattered light in the near infrared. These observations suggest that the surface of the disc around the two outer planets may lack small dust grains ($R_s \lesssim 1\ \mu\text{m}$). Muro-Arena et al. (2018) showed that “enhanced” settling can reproduce observations if the applied turbulence parameter in the region is $\alpha \sim 10^{-5}$, as applied herein. These observations are compatible with (or do not exclude) the presence of collisionally-produced dust in the system since, as mentioned above, the collision frequency of planetesimals reduces as their orbital distance increases. Hence, the supply rate of second-generation dust may fall beneath the removal rate by sedimentation in the region of the outer rings.

5 CONCLUSIONS

HD 163296 is probably one of the most thoroughly studied protoplanetary disc because of its size and complex structure, characterised by well-defined rings and gaps, which possibly originate from either forming or recently-formed giant planets. Past work (Turrini et al. 2019) suggests that orbital excitation of leftover planetesimals by nearby giant planets leads to collisions and to the production of second-generation dust. This process would point to a resurgence of particulate material in circumstellar discs that harbour massive planets, once these planets are nearly fully grown (i.e., at ages $\gtrsim 1\ \text{Myr}$).

The goal of the paper is to test this scenario and investigate the evolution of second-generation dust in the system, under the assumption that said dust is produced by collisional comminution of planetesimals whose orbits have been excited by the embedded planets. Contrary to primordial dust, which is old enough to have settled on near-circular orbits in the disc mid-plane and to have been cleared out of the gaps carved by the planets in the gas distribution, second-generation dust is continuously produced and is more dynamically active, being delivered by collisions to highly eccentric and inclined trajectories.

We present hydrodynamic calculations of the HD 163296 system, simulating both gas and dust components, and applying different initial conditions to the grains, depending on whether they are intended to represent first- or second-generation dust populations. We also consider different approximations for the state of the gaseous disc, based on prior modelling work that tried to reproduce some observational features. Contrary to prior studies of this system that only modelled the mid-plane distribution of dust in two dimensions (e.g., Isella et al. 2016; Liu et al. 2018), we constructed three-dimensional disc models in order to examine the vertical distribution and settling dynamics of grains of various sizes. These are the first 3-D hydrodynamic models of the system (to our knowledge) that include dust and show some important features, such as the formation of vortices induced by Rossby waves (caused by the low levels of turbulence viscosity predicted for the system, e.g., Liu et al. 2018). These vortices are effective in collecting dust in the disc mid-plane and may represent sites for additional planetesimal formation (see, e.g., Heng & Kenyon 2010; Cuzzi et al. 2010), which would contribute to replenish the population of large bodies.

The most noticeable differences between the density distributions of first- and second-generation dust appear in the vertical direction. Second-generation dust is expected to have, on average, higher inclination, with small grains taking longer to settle (than large grains) and therefore extending farther above the mid-plane. Grains produced by collisions of planetesimals are also expected to be injected on highly eccentric orbits which, however, are rapidly circularised. The presence of small grains distributed in the vertical direction is determined by a balance between the rate of sedimentation and the rate of production by collisions (of larger bodies on inclined orbits). We find that the sedimentation rate of $\sim \mu\text{m}$ -size grains is comparable to estimates of the production rate of second-generation dust (Turrini et al. 2019), therefore allowing this population to be persistent and potentially observable. This possibility may reduce as the disc ages and gas disperses since settling timescale would become shorter (as gas densities decline). Large, $\sim \text{mm}$ -size grains would instead settle too quickly to be observable. First-generation dust remains broadly confined to the mid-plane of the disc, although subject to some amount of vertical stirring by the planets.

Production rates of second-generation dust are expected to depend on some specific details (e.g., number density of planetesimals and their size distribution). Assuming we applied representative ranges of parameters for HD 163296, as long as planetesimal collisional timescales are $\lesssim 1.5\ \text{Myr}$, second-generation dust should be distinguishable from primordial dust. If collisional timescales are longer, the two populations would be likely completely mixed. The admixture, largely confined to the disc mid-plane, would not offer distinctive dynamical signatures for separating the two populations. Coagulation and weathering processes would likely smooth compositional differences. Once gas is completely dissipated, collisions among planetesimals may continue but the lifetime of second-generation dust would be mainly dictated by Poynting–Robertson drag and planetesimal scattering timescales.

The behaviour of small, second-generation dust may also aid in the interpretation of some modelling results (e.g., Ohashi & Kataoka 2019), which show that beyond 70 au, outside the location of the innermost planet, the dust scale-height is about twice as large as that of inner disc regions. Ohashi & Kataoka (2019) suggested that an increase in gas turbulence strength at those radial locations, and therefore enhanced vertical stirring, may be responsible for these results. However, collisionally-produced dust may also produce an enhanced disc scale-height of solids in the proximity of the planet’s orbits. Clearly, this latter interpretation would not rule out the possibility of a radial variability of the turbulence strength, but it would rather offer another, or contributing, explanation for the larger dust scale-height observed in some sections of the disc.

Another finding of this work is that second-generation dust particles tend to survive longer within the gaps carved by the planets in the gas distribution. The effect is expected as long as the settling timescales of the grains remain longer than the clearing timescales from the gap regions. This process may offer an additional observational test for the presence of second-generation dust particles.

Although derived for the HD 163296 system, the general conclusion of this study would be applicable to similar systems with embedded giant planets. For example, collisionally-produced grains may be present in the HD 100546 system, which is suspected to harbour a planet at about 70 au from the star, and for which there is observational evidence of dust orbiting at considerable heights over the disc mid-plane (Sissa et al. 2018).

ACKNOWLEDGEMENTS

We thank an anonymous reviewer whose comments helped improve this paper. Primary support for this work was provided by NASA's Research Opportunities in Space and Earth Science (proposals 80HQTR19T0071 and 80HQTR19T0086). Computational resources supporting this work were provided by the NASA High-End Computing (HEC) Program through the NASA Advanced Supercomputing (NAS) Division at Ames Research Center.

DATA AVAILABILITY

The data underlying the research results described in the article will be shared upon reasonable request to the authors.

REFERENCES

- Alibert Y., et al., 2018, *Nature Astronomy*, **2**, 873
 Baraffe I., Chabrier G., Barman T. S., Allard F., Hauschildt P. H., 2003, *A&A*, **402**, 701
 Barge P., Sommeria J., 1995, *A&A*, **295**, L1
 Bracco A., Chavanis P. H., Provenzale A., Spiegel E. A., 1999, *Physics of Fluids*, **11**, 2280
 Cuzzi J. N., Hogan R. C., Bottke W. F., 2010, *Icarus*, **208**, 518
 D'Angelo G., Marzari F., 2012, *ApJ*, **757**, 50
 D'Angelo G., Podolak M., 2015, *ApJ*, **806**, 203
 D'Angelo G., Lubow S. H., Bate M. R., 2006, *ApJ*, **652**, 1698
 D'Angelo G., Weidenschilling S. J., Lissauer J. J., Bodenheimer P., 2021, *Icarus*, **355**, 114087
 Doi K., Kataoka A., 2021, *ApJ*, **912**, 164
 Dubrulle B., Morfill G., Sterzik M., 1995, *Icarus*, **114**, 237
 Dullemond C. P., Dominik C., 2004, *A&A*, **421**, 1075
 Dullemond C. P., Isella A., Andrews S. M., Skobleva I., Dzyurkevich N., 2020, *A&A*, **633**, A137
 Flaherty K. M., Hughes A. M., Rosenfeld K. A., Andrews S. M., Chiang E., Simon J. B., Kerzner S., Wilner D. J., 2015, *ApJ*, **813**, 99
 Fu W., Li H., Lubow S., Li S., 2014, *ApJ*, **788**, L41
 Heng K., Kenyon S. J., 2010, *MNRAS*, **408**, 1476
 Isella A., et al., 2016, *Phys. Rev. Lett.*, **117**, 251101
 Li H., Colgate S. A., Wendroff B., Liska R., 2001, *ApJ*, **551**, 874
 Lissauer J. J., Hubickyj O., D'Angelo G., Bodenheimer P., 2009, *Icarus*, **199**, 338
 Liu S.-F., Jin S., Li S., Isella A., Li H., 2018, *ApJ*, **857**, 87
 Lovelace R. V. E., Li H., Colgate S. A., Nelson A. F., 1999, *ApJ*, **513**, 805
 Marzari F., D'Angelo G., Picogna G., 2019, *AJ*, **157**, 45
 Masset F., 2000, *A&AS*, **141**, 165
 Meheut H., Yu C., Lai D., 2012, *MNRAS*, **422**, 2399
 Mesa D., et al., 2019, *MNRAS*, **488**, 37
 Muro-Arena G. A., et al., 2018, *A&A*, **614**, A24
 Ogilvie G. I., Lubow S. H., 2003, *ApJ*, **587**, 398
 Ohashi S., Kataoka A., 2019, *ApJ*, **886**, 103
 Pinte C., et al., 2018, *ApJ*, **860**, L13
 Rab C., Kamp I., Dominik C., Ginski C., Muro-Arena G. A., Thi W. F., Waters L. B. F. M., Woitke P., 2020, *A&A*, **642**, A165
 Rich E. A., et al., 2019, *ApJ*, **875**, 38
 Rich E. A., Wisniewski J. P., Sitko M. L., Grady C. A., Tobin J. J., Fukagawa M., 2020, *ApJ*, **902**, 4
 Shakura N. I., Sunyaev R. A., 1973, *A&A*, **24**, 337
 Sissa E., et al., 2018, *A&A*, **619**, A160
 Tagger M., 2001, *A&A*, **380**, 750
 Takahashi S. Z., Inutsuka S.-i., 2014, *ApJ*, **794**, 55
 Teague R., Bae J., Bergin E. A., Birnstiel T., Foreman-Mackey D., 2018, *ApJ*, **860**, L12
 Turrini D., Marzari F., Polychroni D., Testi L., 2019, *ApJ*, **877**, 50

- Vioque M., Oudmaijer R. D., Baines D., Mendigutía I., Pérez-Martínez R., 2018, *A&A*, **620**, A128
 Voelkel O., Klahr H., Mordasini C., Emsenhuber A., Lenz C., 2020, *A&A*, **642**, A75
 Weidenschilling S. J., 2010, *ApJ*, **722**, 1716
 Wisniewski J. P., Clampin M., Grady C. A., Ardila D. R., Ford H. C., Golimowski D. A., Illingworth G. D., Krist J. E., 2008, *ApJ*, **682**, 548
 van der Marel N., Williams J. P., Bruderer S., 2018, *ApJ*, **867**, L14

APPENDIX A: DUST DISTRIBUTION SENSITIVITY ON PARTICLE NUMBER AND GRID RESOLUTION

The basic assumption of this study is that dusty particles are distributed above the disc mid-plane by planetesimals colliding at heights $\gtrsim H$, as found in previous work (Turrini et al. 2019). Although we did not model collisions among large bodies, we checked that model configurations used herein are compatible with this assumption in terms of inclination and eccentricity excitation driven by the planets. We performed a calculation based on $\text{H}\alpha 5$ and including bodies ranging in radius between 0.1 and 100 km, initialized on near-circular ($e_s < 0.01$) and non-inclined ($i_s < 0.5^\circ$) orbits. Results show that, after about 600 orbits (at $r = r_0$), 43% of the bodies have $e_s > 0.2$ and 46% have $i_s > H/a_s$, in accord with prior work.

In addition to the initial distribution of grains used in the calculations discussed above (see Section 3.2), we also tested an initial distribution comprising 112000 particles, equally divided in four size bins of radius $R_s = 1 \mu\text{m}$, $10 \mu\text{m}$, $100 \mu\text{m}$, and 1mm . The test is intended to probe the extent to which results may be affected by small-number statistics in some disc regions.

The orbital characteristics of the initial (normalized) distributions are displayed in the top panels of Figure A1. As discussed above, the initial distribution of eccentricities is not important since orbits are circularised relatively quickly. The details of the initial inclination distribution are not expected to affect much the results of the calculations, as long as dust grains are initially present at heights $\gtrsim H$ above the disc mid-plane. The middle and bottom rows of the Figure show the evolution at $t = 2750$ orbits (at $r = r_0$), that is, 250 orbits after the deployment of the solids, for the calculations with lower (middle) and higher (bottom) number of grains. The normalized histograms, including all particles, use the same bin sizes (in the middle and bottom panels) and display similar features for all orbital quantities. Therefore, small-number statistics does not significantly affect the results presented and discussed above.

Two-dimensional dust distributions for the same cases are reported in Figure A2. Results from the calculation with the smaller number of particles are displayed on the left and those with the larger number of particles at the centre. The distributions in the r - θ planes show very similar characteristics. Similar traits also appear in the r - ϕ distributions, which clearly trace the accumulation of grains inside three vortices, exterior to each of the planets' orbit. At this epoch, enhanced concentrations mainly involve 1 mm grains, which have the shortest coupling time with the gas. But smaller grains can also be seen to locally concentrate, especially in the most external vortex. As discussed above, over longer timescales, also $\sim 1 \mu\text{m}$ dust orbiting close to the mid-plane is collected in vortices (see Figures 4, 6 and 8). The emergence of vortices requires low levels of turbulence in the gas (as are predicted for HD 163296, e.g., Liu et al. 2018). The right panel of the Figure shows the dust distributions in a simulation whose setup follows that of model $\text{L}\alpha 6$, but with a higher gas viscosity, corresponding to a turbulence parameter $\alpha = 10^{-3}$. In this case, the dust distribution in the r - ϕ plane clearly points to the absence of vortices in the gas, and 1 mm particles are collected at locations in

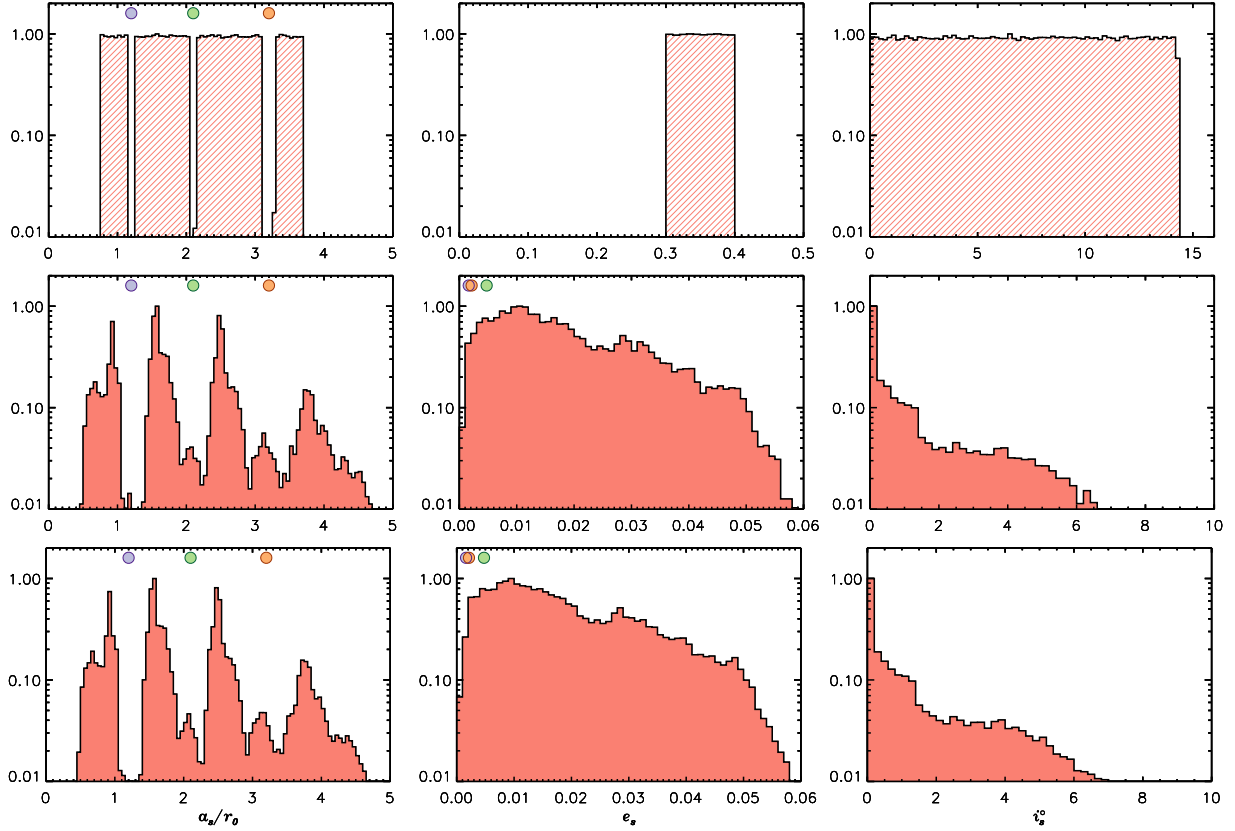


Figure A1. Comparison of histograms with different number of particles from two versions of model Lm α 6. The evolution time is $t = 2750$ orbits (at $r = r_0$) and the solids have evolved for 250 orbits. Top Row: Initial (normalized) dust distributions of semi-major axis (left), orbital eccentricity (centre), and inclination (right) of second-generation dust. Middle row: Normalised distributions from the model with smaller number of particles. Bottom row: Normalised distributions from the model with larger number of particles. The coloured circles represent the planets’ semi-major axis (left panels) and orbital eccentricity (centre panels).

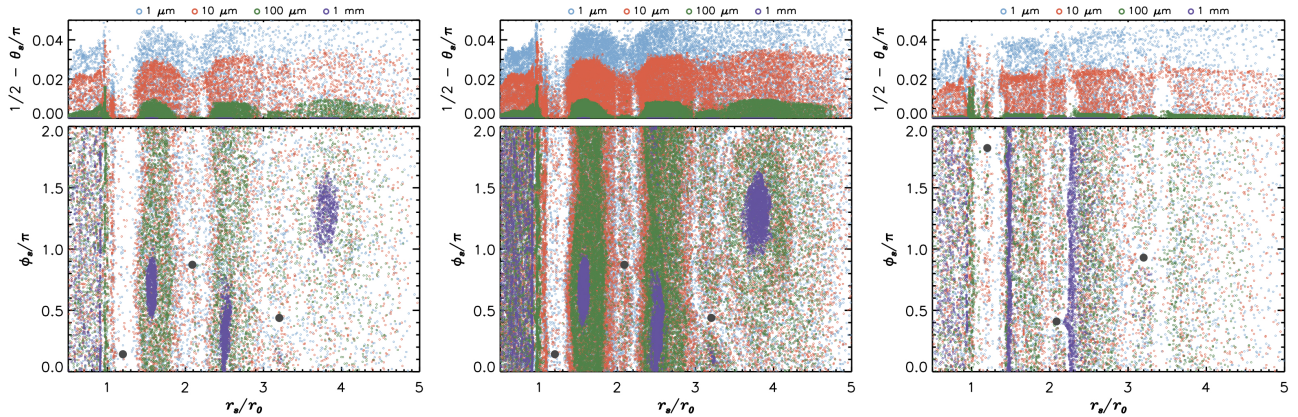


Figure A2. Comparison of the dust distributions, at $t = 2750$ orbits, for the simulations of Figure A1 (case with smaller number of particles on the left and larger number at the centre). Top and bottom panels indicate the particles’ positions projected in the r - θ and r - ϕ planes. Particle radii are colour-coded (see legend); solid circles represent the planets. The right panel refers to a simulation with a setup similar to that of model Lm α 6, but with turbulence parameter $\alpha = 10^{-3}$. (High-resolution versions of this figure can be found [here](#).)

proximity of the edges of the tidal gaps of the two innermost planets, where $\langle u_\phi/u_\phi^* \rangle > 1$.

The three models in Table 1 were also tested at a grid resolution twice as high in each direction ($1332 \times 42 \times 842$ grid elements) as the standard resolution, a factor of 8 enhancement in volume resolution. The hydrodynamic variables from each model (at standard resolu-

tion) were interpolated on the high-resolution grid at the time when particles were deployed and then the high-resolution models were evolved for ≈ 250 orbits at $r = r_0$. Figure A3 displays a comparison of bulk quantities at standard (coloured curves) and high (black curves) resolutions. Both the surface density (2π -averaged around the star, top) and the perturbation on the azimuthal velocity (u_ϕ/u_ϕ^* ,

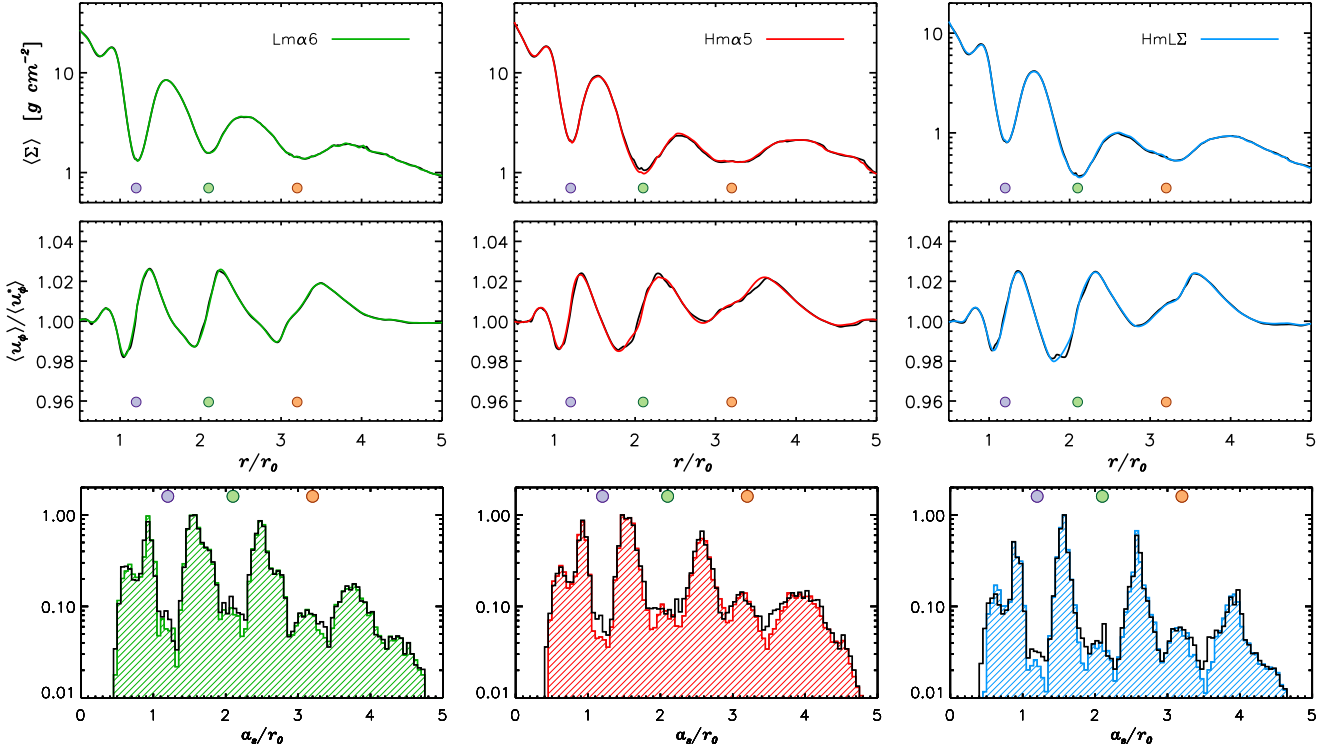


Figure A3. Comparison of models at different resolutions, for the averaged surface density (top), the azimuthal velocity perturbation (middle), and the total dust distribution (bottom), as indicated. The black curves represent the high-resolution calculations (see text for details).

see Section 4, middle) are very similar in each pair of simulations, throughout the disc's region where planets orbit. The bottom panels report the histograms of the total dust distributions, and there is general agreement of the particles' evolution at the two resolutions. Therefore, resolution effects are marginal and likely insignificant in the simulations presented herein.

This paper has been typeset from a \LaTeX file prepared by the author.